PCCP

Accepted Manuscript

ROYAL SOCIETY OF CHEMISTRY

www.rsc.org/pccp

Physical Chemistry Chemical Physics RSCPublishing

ARTICLE

Soft-Template-Carbonization Route to Highly Textured Mesoporous Carbon-TiO_2 Inverse Opals for Efficient Photocatalytic and Photoelectrochemical Applications

Cite this: DOI: 10.1039/x0xx00000x

Received 00th January 2014,
Accepted 00th January 2014

DOI: 10.1039/x0xx00000x

www.rsc.org/

Li Na Quan,[a] Yoon Hee Jang,[ab] Kelsey A. Stoerzinger,[c] Kevin J. May,[b] Yu Jin Jang,[a] Saji Thomas Kochuveedu,[a] Yang Shao-Horn*[bc] and Dong Ha Kim*[ab]

Hierarchically organized mesoporous carbon-TiO_2 inverse opal nanostructures were synthesized by complementary colloid and block copolymer (BCP) self-assembly, where the triblock copolymer P123 acts simultaneously as template and carbon source. Highly ordered mesoporous inverse opal nanostructures with nano-textured surface morphology and multiple-length scale nanopores provide increased light-activated surface area and scattering effects, leading to enhanced photoabsorption efficiency and the transport of matters. UV-vis absorption, X-ray photoelectron spectroscopy and Mott-Schottky measurement studies show that incorporation of carbon moieties into TiO_2 via direct conversion of BCPs creates a new energy level above the valence band of TiO_2, resulting in an effective decrease in the band gap. A significant enhanced visible light photocatalytic activity was demonstrated for the mesoporous carbon-TiO_2 inverse opals in terms of the degradation of *p*-nitrophenol (~79 %) and photoelectrochemical water splitting (~0.087 %).

1 Introduction

Nanostructured semiconductor photocatalysts have been considered essential elements in recent energy conversion and storage as well as environmental remediation. Of the numerous candidates, titanium dioxide (TiO_2) has been recognized as representative photocatalyst due to its good stability, nontoxicity, and UV absorbance.[1] For the enhancement of the photocatalytic efficiency, many efforts have been made to control over the size, morphology, electronic structure and preparation method. In particular, mesoporous structures have been actively studied due to their large accessible surface area and well-defined uniform pore size and excellent connectivity, in which both effective charge carried transfer and efficient mass flow of the reactants are attained.[2, 3] Commercially available amphiphilic poly(ethylene oxide-*block*-propylene oxide-*block*-ethylene oxide) triblock copolymers, typically Pluronic P123, have been widely used as the structure-directing agents for the construction of highly organized mesoporous TiO_2. Three-dimensional (3D) inverse opal structures mediated by colloidal particle assemblies were suggested as another promising class of photocatalysts with high surface area.[4-7] It can be suggested as a photon trapping structure in which the effective optical path length is increased by several times, triggered by scattering effect. For instance, Zhou *et al*.[8] reported that periodically ordered 3D inverse opal photoelectrode films showed much higher photocurrent density than disordered films in the photoelectrochemical water splitting. In this regard, it is an intriguing and crucial task to develop TiO_2 based systems having hierarchically organized high surface area and light trapping effects in order to maximize the photocatalytic efficiency.

However, one of the major drawbacks of TiO_2 is the low efficiency under visible light illumination due to the large band gap (~3.2 eV), corresponding to a threshold wavelength of 388 nm, which inherently limits the activity only under UV light irradiation.[9] For useful utilization of solar energy, the development of visible light-induced photocatalysts is most important. Numerous attempts have been devoted to prepare solar-driven photocatalysts including metal or nonmetal doping,[10-19] coupling of narrow band gap semiconductors,[20, 21] and dye sensitization[22]. In particular, doping with nonmetals such as carbon,[10-15] sulfur,[16] nitrogen[17] is known to modify the electronic structure of TiO_2, thereby narrowing the band gap. Among the various nonmetal dopants, carbon doping has been theoretically claimed to have a potential advantage over other dopings.[23] Carbon-doped TiO_2 nanostructures satisfy the requirement as an efficient photocatalytic material since its conduction band remains above the redox potential and doped carbon moieties act as sensitizers, synergistically leading to wide visible light absorption and high adsorption of organic pollutants facilitating the interface reaction of photocatalysis. However, conventional approaches to incorporate carbon dopants have limitation in that i) addition of external carbon

precursors is required and ii) aggregation of carbon species commonly arises. In our previous study, block copolymers (BCPs) were used simultaneously as soft templates and carbon precursors in the synthesis of hybrid carbonaceous materials.[24-28] Lin *et al.*[14] fabricated TiO_2 photocatalysts doped with uniformly dispersed carbons based on a simple one-step carbonization of a self-assembled matrix consisting of TiO_2 precursor and triblock copolymer P123. As outlined above, it is essential to construct a universal protocol for the generation of hybrid carbon photocatalysts combined with hierarchical structures with high surface area and viable visible light activity.

Herein, we developed hierarchical hybrid carbon-TiO_2 inverse opal nanostructures with mesoporous textures on the surface via complementary colloid templating and direct carbonization of BCP scaffolds, and demonstrated their enhanced photocatalytic activity under UV or visible light illumination. The mesoporous carbon-TiO_2 inverse opal was fabricated using polystyrene (PS) beads and P123 as templates. Key to the advanced feature of the fabrication route proposed in this study includes facile preparation of carbonaceous nanohybrids via direct conversion of BCPs and incorporation of multiple length scale nanopores in the inverse opals. In order to evaluate the photocatalytic activity of thus-obtained samples, the photodegradation of *p*-nitrophenol (PNP) was selected as a model reaction because the compound is considered one of the most refractory substances present in industrial wastewaters with high stability and solubility in water. Photoelectrochemical water splitting was also demonstrated using mesoporous carbon-TiO_2 inverse opals under the visible light irradiation. Thus, the enhanced visible light active photocatalysis is systematically investigated based on a new class of hierarchical mesoporous carbon-TiO_2 nanostructures by optimizing the composition and morphology. The photocatalytic activity of three different types of TiO_2 inverse opals was compared to suggest an optimized nanostructured photocatalyst.

2 Experimental

2.1 Materials

Ethanol, hydrochloric acid (HCl), acetylacetone (Acac) were purchased from DAE JUNG chemical, and styrene, potassium persulfate (PPS), sodium dodecylculfate (SDS), Pluronic P123, tetrabutyl titanate ($Ti(OCH_2CH_2CH_2CH_3)_4$, TBOT, 97 %), *p*-nitrophenol (PNP), potassium hydroxide (KOH) and sodium sulfate (Na_2SO_4) were purchased from Sigma-Aldrich.

2.2 Synthesis of polystyrene (PS) beads

Polystyrene (PS) nanoparticles (NPs) were synthesized by controlled emulsion polymerization. After purging the stabilized DI water under N_2 flow for 30 min, PPS initiators and SDS surfactants were added, followed by quick injection of styrene monomers which had been filtered with alumina. After polymerization at 70˚C for 4 h, PS NPs with an average diameter of about 270 nm were obtained.

2.3 Preparation of precursor solutions

The preparation method of triblock copolymer based TiO_2 sol-gel precursor is described elsewhere.[29] In a typical procedure, commercially available poly(ethylene oxide-block-propylene oxide-block-ethylene oxide) triblock copolymer (P123) (0.58 g) was dissolved in anhydrous ethanol (5.92 g) and HCl (0.29 g), under vigorous stirring for 1 h. Acetylacetone (0.1 g) was then added into this solution and stirred for an additional 20 min. Finally, TBOT (3.4 g) was introduced and the solution was kept for 24 h at room temperature (RT) under stirring. For comparison, TiO_2 sol-gel precursor without P123 was also prepared for the fabrication of neat TiO_2 inverse opals.

2.4 Fabrication of various inverse opals

The colloidal dispersion of the PS opals was drop-cast and assembled on a glass substrate and dried in the convention oven at 60˚C. Hexagonally packed PS opal film was then placed at 90˚C for 1h to introduce moderate necking between spheres. This step was found to improve the adhesion and structural stability of the resultant TiO_2 inverse opal films. The substrate with PS opal template was carefully immersed vertically into a mixture solution of P123 and TiO_2 precursors for 5 min to let the solution infiltrate into the close packed PS opals. After the poured template was dried at RT for 24 h, the sample was thermally treated at 90˚C for 24 h to consolidate the inorganic network. Finally, mesoporous TiO_2 inverse opals were obtained by heating the sample at 400˚C under ambient condition. On the other hand, the poured template was exposed to UV light (λ = 254 nm) at RT for 1 h under vacuum condition and then subsequently carbonized at 600˚C in Ar atmosphere for 1h in order to generate hybrid mesoporous carbon-TiO_2 inverse opal structures. For comparison, TiO_2 inverse opal structures without mesopores were also prepared by calcining the P123 template free samples at 400 ˚C for 3 h under air atmosphere.

2.5 Instruments and measurements

The surface morphology was characterized by scanning electron microscopy (SEM; JEOL JSM6700-F). For the elemental analysis, energy-dispersive X-ray spectroscopy (EDX) was performed on a JEOL JEM-3011 at an accelerating voltage of 200 kV. The crystalline structure of the neat TiO_2 inverse opal, mesoporous TiO_2 inverse opal and carbon-TiO_2 inverse opal were investigated by X-ray diffraction (XRD) Cu-Kα radiation (D/max RA, Rigaku Co.). Raman scattering spectra were recorded on a T64000 (HORIABA Jobin Yvon, France). The specific surface area and pore diameter distribution of the present structures were examined by measuring nitrogen adsorption–desorption isotherms with ASAP 2020 adsorption analyzer at 77 K. All the present samples were degassed at 180˚C for 12 h under vacuum before the adsorption measurement. UV-vis absorbance and diffuse reflectance spectra were measured using a Sinco S-4100 spectrometer. X-ray photoelectron spectroscopy (XPS) was measured with a Thermo Scientific K-Alpha XPS, using a dual beam source and ultra-low energy electron beam for charge compensation. The energy scale was calibrated such that 0 eV reflects the position of the Fermi level, by defining the adventitious carbon peak as 284.8 eV.[30] The TGA–DTA curve was recorded on TA instrument SDT Q600 (TA instrument, USA). The temperature was increased from ambient to 900℃ at a heating rate of 10℃/min under airflow. Mott-Schottky measurements were performed in 3M KCl at 1 kHz using electrochemical analyser, IVIUMSTAT.XR, IVIUM Technologies.

2.6 Photocatalytic measurements

The photocatalytic degradation of the organic compound on neat TiO_2, mesoporous TiO_2 and carbon-TiO_2 inverse opals were tested both under the UV (λ = 254 nm) and visible light irradiation. For the catalytic measurements, the sample was obtained by gently scraping the film off the glass substrates, and 10 ppm of PNP was prepared in 30 ml water. The solution containing powder sample was kept under stirring. The experimental setup was irradiated using a Xe lamp (Newport Co. Ltd, Model 66984) equipped with a 420 nm cut-off filter at a power of 450 W as a visible light source. The decrease in the absorbance of the characteristic peak of PNP was monitored by UV-vis spectroscopy (Varian Cary5000 UV-vis-NIR spectrophotometer). The photoelectrochemical (PEC) measurements were done using mesoporous carbon-TiO_2 inverse opals on ITO as a working electrode, a platinum foil as a counter electrode and Ag/AgCl or SCE as a reference electrode, respectively, in a 0.5 M KOH or 0.1 M Na_2SO_4 electrolyte deaerated by purging N_2 gas into the electrolyte. The light emitted from a Xe lamp passed through the window and was irradiated directly onto the TiO_2 photoelectrode.

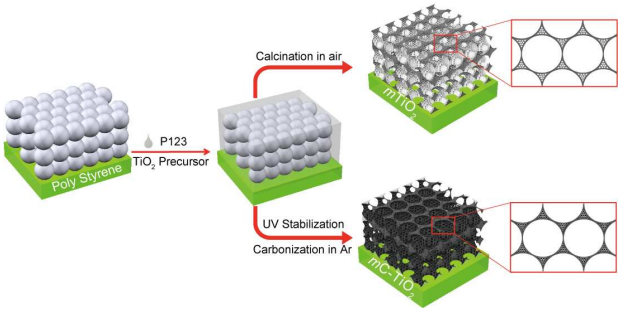

Scheme 1. Schematic representation of the fabrication of *m*TiO_2 and *m*C-TiO_2 inverse opals. 3D PS bead arrays were prepared first using colloid self-assembly and a common solution consisting of P123 and TiO_2 precursors were infiltrated through the interstitial sites of the PS template. The samples were either calcined under air atmosphere (upper route) or subjected to sequential UV exposure in vacuum followed by calcination in Ar atmosphere (lower route) to obtain *m*TiO_2 and *m*C-TiO_2 inverse opals, respectively. The resulting inverse opals contain well defined, periodic mesopore arrays as a result of the phase separation between the constituent blocks of P123 and removal of polymer templates.

3 Results and Discussion

Scheme 1 shows the entire procedure to fabricate the 3D mesoporous TiO_2 (*m*TiO_2) and carbon-TiO_2 (*m*C-TiO_2) inverse opal nanostructures. 3D PS bead arrays were prepared first using colloid self-assembly (Figure S1a) and a common solution consisting of P123 and TiO_2 precursors were fully infiltrated through the interstitial sites of the PS template (Figure S1b). After infiltration with the mixture solution, the samples were either calcined at 400˚C under air atmosphere or subjected to sequential UV exposure in vacuum followed by calcination at 600˚C in Ar atmosphere to obtain *m*TiO_2 and *m*C-TiO_2 inverse opals, respectively. It is clearly observed that nanoscale pores were generated at the TiO_2 and carbon-TiO_2 framework as shown in Figure 1a and 1b as a result of the phase separation between the constituent blocks of P123 and removal of polymer templates. The difference in color due to the presence of carbon can be discerned with the naked eye as can be compared from the microscopic images (insets in Figure 1). It is also found that the average wall thickness of the *m*C-TiO_2 framework is thinner than that of the *m*TiO_2, implying that volume shrinkage occurred during the carbonization step. For comparison, neat TiO_2 inverse opal structures without mesopores were also prepared by calcining the P123 template free samples (Figure S1c).

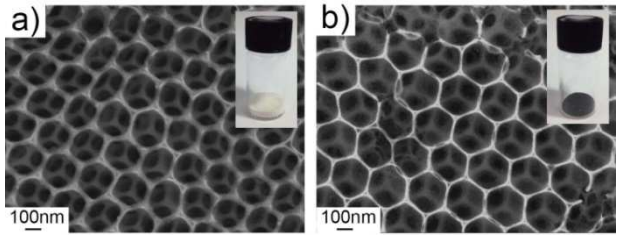

Figure 1. Field emission scanning electron microscopy (FESEM) images of a) *m*TiO_2 and b) *m*C-TiO_2 inverse opals. Insets are the corresponding photographs of the resulting samples.

The crystalline phase of neat TiO_2, $m$$TiO_2$ and mC-TiO_2 inverse opals was investigated by XRD patterns as shown in Figure 2, where all peaks match the typical diffraction pattern of an anatase TiO_2 (JCPDS, No. 21-1272). To confirm the presence and physicochemical nature of carbon moieties derived from calcination of P123 in the composite TiO_2 structures, Raman spectroscopy and energy-dispersive X-ray spectroscopy (EDX) measurements were performed. In the Raman spectrum of mC-TiO_2 (Figure 2b), the position of G band at about 1600 cm^{-1} is in line with the presence of nanocrystalline carbons attributed to a high content of sp^2-hybridized carbon and D band at about 1350 cm^{-1} corresponds to the defects of disordered carbon, which indicates that P123 template was converted into a partially graphitic carbon.[31] Figure S3 shows the Raman spectra of the neat TiO_2 and $m$$TiO_2$ inverse opals. The EDX result also confirms the presence of carbon moieties (see Figure S2 in the supporting information).

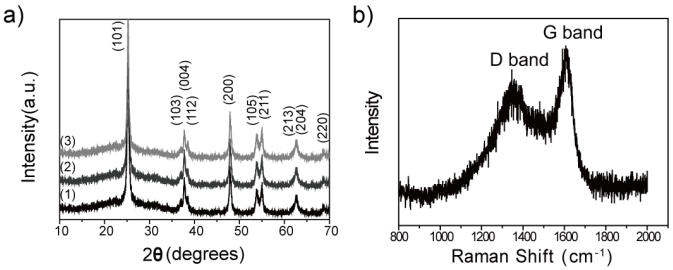

Figure 2. a) XRD patterns of 1) neat TiO_2, 2) $m$$TiO_2$ and 3) mC-TiO_2 inverse opals. b) Raman spectrum of mC-TiO_2 inverse opals.

Thermogravimetric analysis (TGA) measurement was carried out to further confirm the carbon content in the composite (see Figure S4 in the supporting information). The mC-TiO_2 inverse opal shows 12 wt% weight loss in the range of 30-400 ℃. It suggests that the content of carbon is roughly 12 wt%. In contrast, the weight loss of neat TiO_2 and $m$$TiO_2$ inverse opals were less than 2 wt%, due to the presence of ash in the samples.

The optical property and the band gap energy of neat TiO_2, $m$$TiO_2$ and mC-TiO_2 inverse opals were investigated by UV-Vis DRS measurements as shown in Figure 3. The distinct difference in absorption characteristics of neat TiO_2, $m$$TiO_2$ and mC-TiO_2 evidences that carbon was doped into TiO_2 nanostructures (Figure 3a). The band gap energy was estimated from the intercept of tangents with the x-axis in Kubelka-Munk plot (Figure 3b).[32] mC-TiO_2 shows a relatively lower band gap energy (~2.9 eV) compared with $m$$TiO_2$ (~3.1 eV) or neat TiO_2 (~3.2 eV) owing to the additional electronic state above the valence band of TiO_2, which contributes to the visible light absorption of TiO_2.[24, 25]

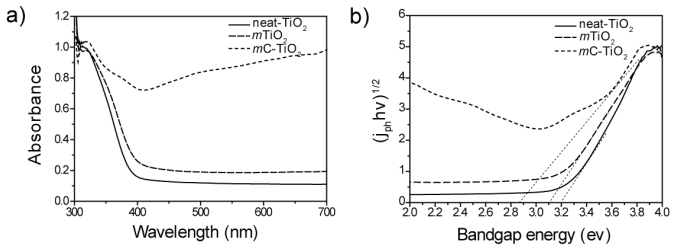

Figure 3. a) UV-Vis absorbance spectra and b) Kubelka-Munk polts of neat TiO_2, $m$$TiO_2$ and mC-TiO_2 inverse opals.

Information about the interaction between carbon and the TiO_2 lattice can be obtained from chemical shifts in photoelectrons from the C 1s core level, as shown in Fig. 4a. Adventitious carbon (hydrocarbons) are ubiquitously present in XPS (located at 284.8 eV),[30] however the extent of oxidized carbon and its chemical shift varies amongst samples. The mC-TiO_2 shows more C-O-C species (located at 286.2 eV)[33] in comparison to either the neat TiO_2 or $m$$TiO_2$ materials, suggesting carbon is well-incorporated into the oxide lattice of the mC-TiO_2. XPS can also measure shifts in the valence band relative to the Fermi level, as shown in Fig. 4b. Although defining an absolute band edge from XPS is challenging due to cross-sectional differences amongst atoms, the valence band of mC-TiO_2 definitively does not shift toward the Fermi level, but in fact shifts away. This suggests the addition of carbon acts as an n-type dopant, and makes mC-TiO_2 degenerate in character, in good agreement with the black color of the powder.

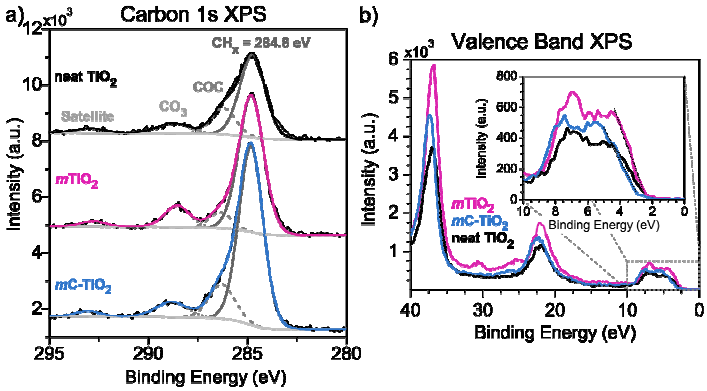

Figure 4. XPS spectra for the a) carbon 1s peak and b) valence band of the neat TiO_2, $m$$TiO_2$ and mC-TiO_2 inverse opal samples. All spectra are calibrated to the adventitious carbon (CH_x) peak at 284.8 eV. Spectra in a) share the same scale and are offset for visibility. Inset in b) shows a magnified view of the valence band near the Fermi level.

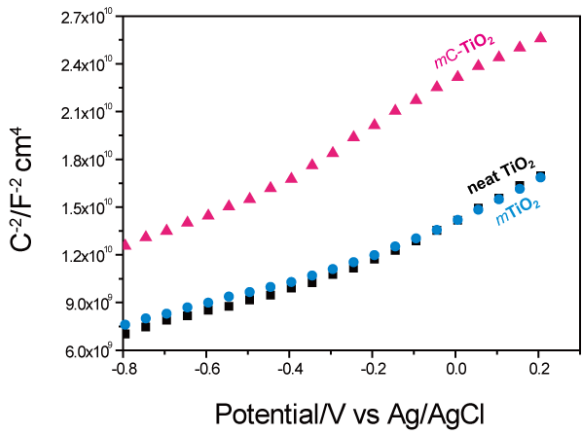

Figure 5. Mott-Schottky plots of neat TiO_2, $m$$TiO_2$ and mC-TiO_2 inverse opals in 3M KCl solution (Ag/AgCl reference electrode) at 1 kHz.

To further characterize the valence and conduction band edge of neat TiO_2, $m$$TiO_2$ and mC-TiO_2 inverse opals, Mott-Schottky plot was obtained (Figure 5). The Fermi level of an n-type semiconductor is defined in accordance with the flat band potential (V_{fb}), and the position of the valence band and conduction band edge of a given semiconductor can be obtained by photoelectrochemical method.[34] The flat band potential (V_{fb}) calculated from the x intercept of linear region, is found to be -0.638, -0.685, -1.082V versus Ag/AgCl for neat TiO_2, $m$$TiO_2$ and mC-TiO_2 inverse opals, respectively. Compared with the neat TiO_2 and $m$$TiO_2$ inverse opals, the V_{fb} of the mC-TiO_2 inverse opal is shifted to a more negative value by 0.4 V. The results indicate that Fermi level of the composite was shifts closer to the conduction band of the semiconductor, which is consistent with the optical and XPS measurements.[35, 36]

Table 1. Calculated average pore size, volume of mesopores and specific surface area for neat TiO_2, $m$$TiO_2$ and mC-TiO_2 inverse opals.

Sample	Pore size (nm)	Pore vol. (cm^3/g)	Surface area (m^2/g)
neat-TiO_2	6.2	0.1	56.6
$m$$TiO_2$	6.5	0.2	114.4
mC-TiO_2	4.7	0.1	75.1

N_2 adsorption-desorption measurements were performed to evaluate the specific surface area and pore size distributions of the three types of samples.[37] The specific surface area (S_{BET}), pore volume and pore size of the samples are listed in Table 1. S_{BET} for neat TiO_2, $m$$TiO_2$ and mC-TiO_2 inverse opals was determined to be ~56.6, 114.4 and 75.1 m^2/g, respectively, as calculated by the multipoint Brunauer–Emmett–Teller (BET) method (inset in Figure 6). All the adsorption curves display H2 type hysteresis loops and type IV isotherms with a sharp capillary condensation step at the range of 0.5 ~ 0.7 relative pressure (P/P_o) of adsorbate gas. The H2 type hysteresis loop is a characteristic of typical mesoporous materials with narrow pores.[38] The $m$$TiO_2$ inverse opal shows the largest specific surface area compared with the neat TiO_2 or mC-TiO_2 inverse opals. The previous SEM images and elemental analysis results evidence this observation, i.e., the P123 was completely removed during the calcination step for the $m$$TiO_2$ inverse opal, leading pores behind, while a significant amount of carbon moieties remained for the mC-TiO_2, exhibiting lower specific surface area. The pore diameter of neat TiO_2, $m$$TiO_2$ and mC-TiO_2 inverse opals are determined to be ~6.2, 6.5 and 4.7 nm, respectively (Figure 6), indicating that the etching of the P123 templates led to a narrow distribution of pores and carbonization induced the decrease in pore size due to overall shrinkage of the system.

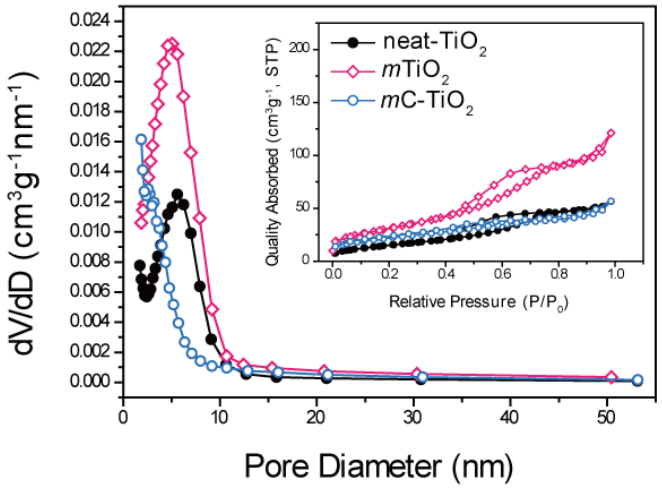

Figure 6. Pore diameter distribution and N_2 adsorption isotherms (inset) for neat TiO_2, $m$$TiO_2$ and mC-TiO_2 inverse opals.

The photocatalytic activity of neat TiO_2, $m$$TiO_2$ and mC-TiO_2 inverse opals under UV light (λ = 254 nm) illumination were evaluated first in terms of the degradation of PNP. The decrease in the absorbance of characteristic peak of PNP at 400 nm was monitored for each of the samples as displayed in Figure 7a-c. The peak at 320 nm is also attributed to the PNP. The adsorption of PNP onto TiO_2 for 1 h in dark served as control, which is denoted as 'Dark' in Figure 7d. The results show that the maximum value decreases after exposure of UV light for 1hr as a result of the PNP degradation. It was found that $m$$TiO_2$ and mC-TiO_2 inverse opals exhibit higher photocatalytic activities compared with neat TiO_2 inverse opal as apparently evidenced by the rapid decrease in peak intensity. For quantitative comparison, the efficiency of the PNP degradation as a function of time was displayed by normalizing the absorbance values of the analytical samples with respect to the initial values (Figure 7d). In the presence of $m$$TiO_2$ or mC-TiO_2 inverse opal, the degradation of PNP was significantly enhanced and more than 71% or 79 % of PNP was completely decomposed after 1h. Highly ordered mesostructures in $m$$TiO_2$ inverse opal can enhance the effective light-activated surface area and allow rapid diffusion of reactants and products, which improve the photoabsorption efficiency and the transport of matters. Thus it shows enhanced photocatalytic activity than neat TiO_2 inverse opal. Even though smaller surface area was observed in mC-TiO_2 inverse opal, it shows improved photocatalytic activity by effective separation of photoelectrons and holes due to the presence of carbon species.[39]

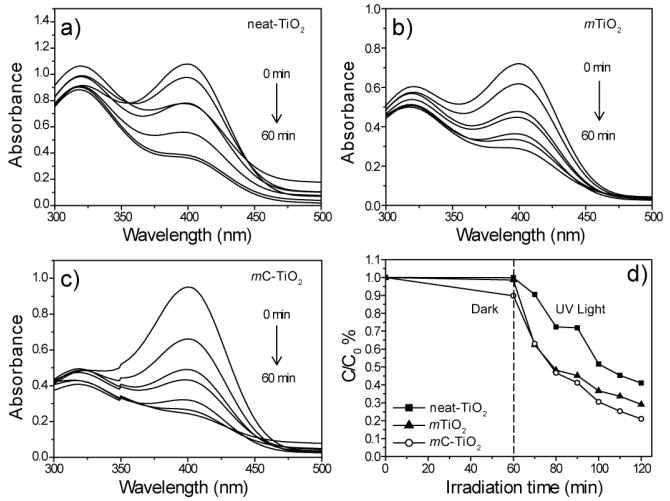

Figure 7. Photocatalytic degradation of PNP using a) neat TiO_2, b) $m$$TiO_2$, and c) mC-TiO_2 inverse opals under UV light. The initial height of the absorbance maximum at around 400nm in the absorbance spectrum of PNP prior to irradiation with UV light was used as reference. Decrease of the peak height was assumed to correspond to the relative decrease in PNP concentration.; d) decolorization efficiency vs. time curves.

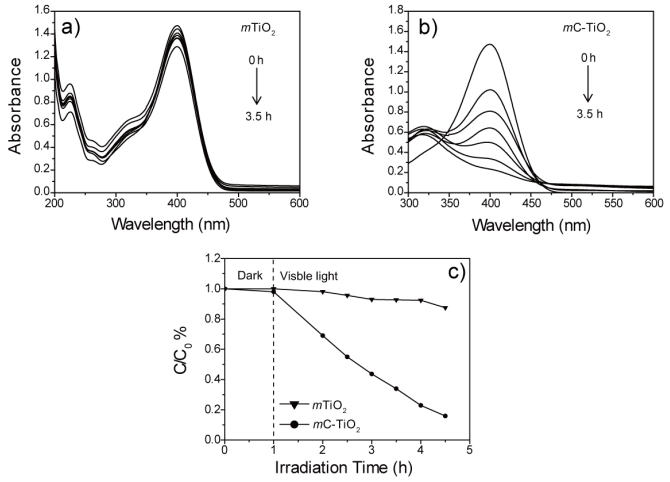

Figure 8. Visible light driven photocatalytic degradation of PNP using a) $m$$TiO_2$ and b) mC-TiO_2 inverse opals. c) Plot of concentration change of PNP versus reaction time in the presence of photocatalysts.

Next, we explore the photocatalytic activity of the samples under visible light illumination. The neat TiO_2 inverse opal did not show any noticeable visible light activity (data not shown). Figure 8a-b depicts a series of spectra measured on the $m$$TiO_2$ and mC-TiO_2 inverse opals, where the maximum intensity of the characteristic peak of PNP at λ~400 nm decreased with increasing the irradiation time. The plots of the logarithm of C/C_0 versus irradiation time were displayed in Figure 8c. It was observed that the $m$$TiO_2$ inverse opal showed negligible photocatalytic ability during 3.5 h illumination due to the inherently wide band gap. On the contrary, the mC-TiO_2 inverse opal exhibits remarkably higher visible light photocatalytic activity than $m$$TiO_2$ inverse opal. It was found that about 66 % of PNP was photodegraded within 3.5 h, implying that incorporation of carbon moieties is responsible for the visible light driven photocatalytic performance. Excitation by low energy photons for the mC-TiO_2 inverse opals is ascribed to the reduced band gap as confirmed by the optical investigation and the carbon networks on the surface may act as a channel to divert excitons from the conduction band of TiO_2, thereby decreasing the rate of recombination. It is assumed that the degradation of PNP is not complete, considering that the peak at 320 nm is still present after 3.5 h. All of the photocatalytic activity results with erro bar are shown in supporting information Figure S5.

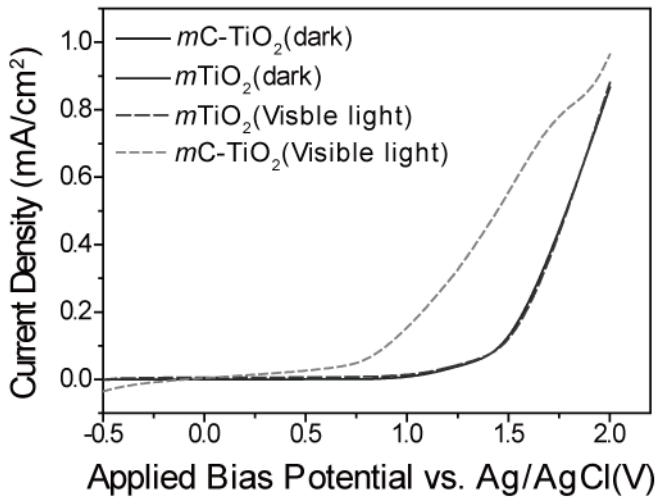

Figure 9. J-V curves plotted for $m$$TiO_2$ and mC-TiO_2 inverse opals in the dark and visible light at a scan rate of 20 mV/s in 0.5 M KOH electrolyte. The potential was measured against the Ag/AgCl reference electrode.

Water splitting via photoelectrochemical (PEC) reaction has gained tremendous attention regarding solar fuel generation and the facile fabrication of cost-effective, viable, and highly efficient visible light active photocatalysts is the key to resolve this critical issue. In order to demonstrate the potential use of the samples as photoanodes, PEC measurements were carried out on $m$$TiO_2$ and mC-TiO_2 inverse opals in a three-electrode system (Figure 9). The inverse opal films on ITO substrate and Pt wire were used as the working electrode and counter electrode, respectively. Ag/AgCl or saturated calomel electrode (SCE) were selected as the reference electrode. The photocurrent density *versus* applied voltage curves were monitored in the dark and under visible light irradiation. The dark scan from -0.5 to 2.0 V *versus* Ag/AgCl showed almost negligible current for $m$$TiO_2$ and mC-TiO_2 inverse opals, whereas under the irradiation of visible light, mC-TiO_2 inverse opal yielded a maximum photocurrent density of 0.29 $mAcm^{-2}$ at 1.2 V. The efficiency (η) for PEC measurements can be calculated by the following relation:

$$\eta = I(1.23\text{-}V_{app})/P_{light} \quad (1)$$

where, I is the measured current density, V_{app} is the applied voltage and P_{light} is the power density of the irradiation. Overall, the maximum efficiency of mTiO$_2$ and mC-TiO$_2$ inverse opals were 0.009 % and 0.087 % respectively, indicating that an enhancement by 9.67 times was obtained for the mC-TiO$_2$ compared with mTiO$_2$ inverse opal.

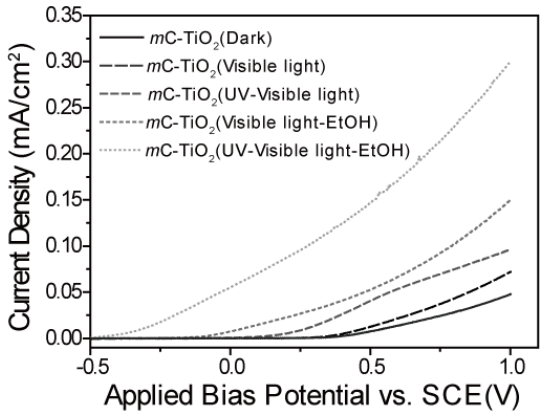

Figure 10. J-V curves plotted for the influence of sacrificial agents (EtOH) on photocurrent using mTiO$_2$ and mC-TiO$_2$ inverse opals in the dark and under visible or UV-visible light at a scan rate of 20 mV/s in 0.1 M Na_2SO_4 electrolyte. The potential was measured against the SCE reference electrode.

As a second model reaction, linear-sweep voltammograms of mC-TiO$_2$ inverse opal/ITO film in Na_2SO_4 electrolyte with or without ethanol were obtained as shown in Figure 10. In normal photocatalytic water splitting systems, oxidation half-reaction proceeds slowly and is required to be speeded up for efficient hydrogen production through the usage of sacrificial reagents such as ethanol, which can facilitate hole consumption and slow down electron–hole recombination so that dramatically enhance hydrogen evolution by several orders of magnitude.[40] In addition, solvent polarity can affect the dissociative adsorption of the ethanol over a pair of Ti and O, which can be considered as the controlling step in the photoreaction on the surface as follows:

$$\text{Et–O–H(a)} + \text{Ti(s)–O(s)} \rightarrow \text{Et–O–Ti(s)} + \text{H–O(s)} \qquad (2)$$

where (a) and (s) indicate adsorbed species and surface, respectively.[41] When the ethanol was added into the electrolyte, the photocurrent was significantly increased under visible or UV-visible light irradiation. When ethanol is included, the photocurrent density generated on the mC-TiO$_2$ inverse opal at 1.00 V *versus* SCE is more than 2 times greater than that of the initial value, only under visible light illumination (Figure 10). Furthermore, when the mC-TiO$_2$ inverse opal was illuminated by UV-visible light, the photocurrent density is increased by ~3.12 times compared with the system without ethanol additives. According to the reactions (3) and (4), the ethanol molecule acts as a "hole" trap itself, where the adsorbed molecule becomes a radical ethoxide and then converted into the carbonyl compound. More electrons were generated when ethanol exists in the electrolyte and these electrons could be rapidly transferred to the cathode together with the photogenerated electrons through the circuit driven by the external bias potential for hydrogen production.[42]

$$h^+ + CH_3CH_2OH \rightarrow CH_3COOH + H^+ + e^- \qquad (3)$$

$$2OH\cdot + CH_3CH_2OH \rightarrow CH_3CHO + 2H_2O + 2e^- \qquad (4)$$

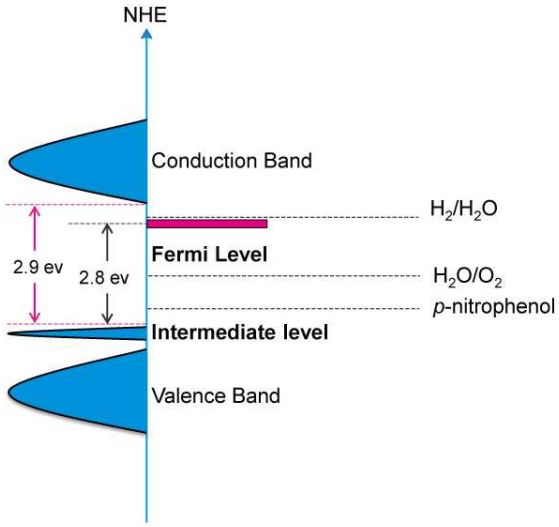

Figure 11. Relative energy diagram of mC-TiO$_2$ inverse opal with respect to the reaction potentials.

On the basis of UV-Vis DRS and XPS study, the relative energy band diagram was schematically depicted as shown in Figure 11. The direct band gap of mC-TiO$_2$ inverse opal (~2.9 ev) was estimated from the Kubelka-Munk plot in Figure 3. From the valence band XPS measurements (Figure 4b), the gap between the valence band (VB) and the Fermi level of mC-TiO$_2$ inverse opal was evaluated as ~2.8 eV. The peak at 286.2 eV in the C 1s spectrum (Figure 4a) can be ascribed to the formation of oxygenated carbon species (Ti-O-C bond), which creates a new intermediate level above the VB of TiO$_2$ through the hybridization of O 2p and C 2p orbitals. The formation of oxygenated carbon species could cause an obvious long-tail absorption in the visible region.[43] For comparison the energy band diagrams of neat TiO$_2$ and mTiO$_2$ inverse opals were also constructed (see Figure S6 and S7 in the supporting information). The potential for the photocatalytic oxidation of PNP was reported to be around 1.3-1.6V vs NHE.[44] It is noted that the ethanol oxidation potential ranges 1.0-0.8 eV vs. NHE.[45]

The factors contributing to the above enhanced photocatalytic activity include i) extension of excitation wavelength through the formation of chemical bonding between the TiO$_2$ and carbon, which is analogous to the doping effect, and ii) the improved dispersion of mC-TiO$_2$ inverse opal that allows for a larger amount of exposed active sites for reactions.

4 Conclusions

We suggested a simple protocol for the fabrication of mesoporous carbon-TiO_2 inverse opal nanostructures using PS beads and self-assembled triblock copolymer (Pluronic P123) as templates. The carbon doping was achieved by direct conversion of polymer scaffolds via sequential UV-stabilization of P123 in vacuum and calcination at elevated temperature. Valid photocatalytic activities for the mesoporous carbon-TiO_2 inverse opal nanostructures were demonstrated in terms of the degradation of PNP and photoelectrochemical measurements under UV or visible light irradiation. Highly ordered mesoporous inverse opal structures provide maximized specific surface area, and the interconnected inverse opals can optimize the transportation of matters and reduce transport limitations. The carbon moieties incorporated into the TiO_2 lattice exists as a oxygenated carbon species, which is responsible for multifunctional advantages such as the improved electron transport, increased visible light absorption, improved photocatalyst dispersion and effective decrease in the band gap energy. The best catalytic activity was obtained on *m*C-TiO_2 inverse opal in terms of the degradation of PNP within 3.5 h under visible light irradiation and the maximum photocurrent density of 0.29 $mAcm^{-2}$ at 1.2 V, corresponding to 0.087 % photoelectrode efficiency. As a whole, the new class of hybrid carbon based hierarchical mesoporous inverse opal structures developed in this study can find great potential in photophysical applications such as photocatalytic degradation of hazardous materials, water splitting for solar fuel production, and photovoltaic and photoelectrochemical cells.

Acknowledgements

This work was supported by National Research Foundation of Korea Grant funded by the Korean Government (2011-0030255; 2011-0029409). This work was performed in part at the Center for Nanoscale Systems (CNS), a member of the National Nanotechnology Infrastructure Network (NNIN), which is supported by the National Science Foundation under NSF award no. ECS-0335765. CNS is part of Harvard University. D. H. Kim appreciates the financial support from the Supporting Program for Professors' Overseas Research funded by LG Yonam Foundation. The authors are grateful to Prof. S. Yoon and H.-Y. Shin for the measurement of Raman spectrum.

Notes and references

[a]Department of Chemistry and Nano Science, Global Top 5 Research Program, Division of Molecular and Life Sciences, College of Natural Sciences, Ewha Womans University, 52, Ewhayeodae-gil, Seodaemun-gu, Seoul 120-750, Korea
[b]Department of Mechanical Engineering, Massachusetts Institute of Technology, 77 Massachusetts Ave, Cambridge, Massachusetts 02139, United States
[c]Department of Materials Science and Engineering, Massachusetts Institute of Technology, 77 Massachusetts Ave, Cambridge, Massachusetts 02139, United States
[*]To whom correspondence should be addressed:
Tel.: +82-2-3277-4517 (D. H. Kim); +1-617-253-2259 (Y. Shao-Horn)
Fax: +82-2-3277-4546 (D. H. Kim); +1-617-258-7018 (Y. Shao-Horn)
E-mail: dhkim@ewha.ac.kr (D. H. Kim); shaohorn@mit.edu (Y. Shao-Horn)

Electronic Supplementary Information (ESI) available: [details of any supplementary information available should be included here]. See DOI: 10.1039/b000000x/

1. X. Chen and S. S. Mao, *Chemical reviews*, **2007**, 107, 2891-2959.
2. J. H. Pan, X. Zhao and W. I. Lee, *Chemical Engineering Journal*, **2011**, 170, 363-380.
3. Y. Ye, C. Jo, I. Jeong and J. Lee, *Nanoscale*, **2013**, 5, 4584-4605.
4. J. Zhao, P. Wan, J. Xiang, T. Tong, L. Dong, Z. Gao, X. Shen and H. Tong, *Microporous and Mesoporous Materials*, **2011**, 138, 200-206.
5. G. Liao, S. Chen, X. Quan, H. Chen and Y. Zhang, *Environmental science & technology*, **2010**, 44, 3481-3485.
6. K. Kim, P. Thiyagarajan, H. Ahn, S. Kim and J. Jang, *Nanoscale*, **2013**.
7. W. Liu, B. Zou, J. Zhao and H. Cui, *Thin Solid Films*, **2010**, 518, 4923-4927.
8. M. Zhou, H. B. Wu, J. Bao, L. Liang, X. W. Lou and Y. Xie, *Angewandte Chemie International Edition*, **2013**, 52, 8579-8583.
9. A. Fujishima, T. N. Rao and D. A. Tryk, *Journal of Photochemistry and Photobiology C: Photochemistry Reviews*, **2000**, 1, 1-21.
10. S. U. Khan, M. Al-Shahry and W. B. Ingler, *Science*, **2002**, 297, 2243-2245.
11. Y. Zhang, P. Xiao, X. Zhou, D. Liu, B. B. Garcia and G. Cao, *Journal of Materials Chemistry*, **2009**, 19, 948-953.
12. C. Xu, R. Killmeyer, M. L. Gray and S. U. Khan, *Applied Catalysis B: Environmental*, **2006**, 64, 312-317.
13. W. Ren, Z. Ai, F. Jia, L. Zhang, X. Fan and Z. Zou, *Applied Catalysis B: Environmental*, **2007**, 69, 138-144.
14. Y.-F. Lee, K.-H. Chang, C.-C. Hu and K.-M. Lin, *Journal of Materials Chemistry*, **2010**, 20, 5682-5688.
15. S. Sakthivel and H. Kisch, *Angewandte Chemie International Edition*, **2003**, 42, 4908-4911.
16. T. Ohno, M. Akiyoshi, T. Umebayashi, K. Asai, T. Mitsui and M. Matsumura, *Applied Catalysis A: General*, **2004**, 265, 115-121.
17. F. Peng, L. Cai, H. Yu, H. Wang and J. Yang, *Journal of Solid State Chemistry*, **2008**, 181, 130-136.
18. S. Anandan and M. Miyauchi, *Physical Chemistry Chemical Physics*, **2011**, 13, 14937-14945.
19. H. Chen, W. Wen, Q. Wang, J. C. Hanson, J. T. Muckerman, E. Fujita, A. I. Frenkel and J. A. Rodriguez, *The Journal of Physical Chemistry C*, **2009**, 113, 3650-3659.
20. L. Wu, J. C. Yu and X. Fu, *Journal of molecular catalysis A: Chemical*, **2006**, 244, 25-32.
21. W. Ho and J. C. Yu, *Journal of Molecular Catalysis A: Chemical*, **2006**, 247, 268-274.
22. J. Jiang, X. Zhang, P. Sun and L. Zhang, *The Journal of Physical Chemistry C*, **2011**, 115, 20555-20564.
23. H. Wang and J. Lewis, *Journal of Physics: Condensed Matter*, **2006**, 18, 421.

24. S. T. Kochuveedu, Y. H. Jang, Y. J. Jang and D. H. Kim, *Journal of Materials Chemistry A*, **2013**, 1, 898-905.
25. S. T. Kochuveedu, Y. J. Jang, Y. H. Jang, W. J. Lee, M.-A. Cha, H. Shin, S. Yoon, S.-S. Lee, S. O. Kim and K. Shin, *Green Chemistry*, **2011**, 13, 3397-3405.
26. Y. J. Jang, Y. H. Jang, M. Steinhart and D. H. Kim, *Chemical Communications*, **2012**, 48, 507-509.
27. Y. H. Jang, S. T. Kochuveedu, Y. J. Jang, H.-Y. Shin, S. Yoon, M. Steinhart and D. H. Kim, *Carbon*, **2011**, 49, 2120-2126.
28. Y. J. Jang, Y. H. Jang, S.-B. Han, D. Khatua, C. Hess, H. Ahn, D. Y. Ryu, K. Shin, K.-W. Park and M. Steinhart, *ACS nano*, **2012**, 7, 1573-1582.
29. Y. Fu, Z. Jin, W. Xue and Z. Ge, *Journal of the American Ceramic Society*, **2008**, 91, 2676-2682.
30. P. Swift, *Surface and Interface Analysis*, **1982**, 4, 47-51.
31. A. Ferrari and J. Robertson, *Physical review B*, **2000**, 61, 14095.
32. H. Lin, C. P. Huang, W. Li, C. Ni, S. I. Shah and Y.-H. Tseng, *Applied Catalysis B: Environmental*, **2006**, 68, 1-11.
33. D. Briggs and G. Beamson, *Analytical chemistry*, **1992**, 64, 1729-1736.
34. M. Grätzel, *Nature*, **2001**, 414, 338-344.
35. F. Zhu, P. Zhang, X. Wu, L. Fu, J. Zhang and D. Xu, *ChemPhysChem*, **2012**, 13, 3731-3737.
36. V. Subramanian, E. E. Wolf and P. V. Kamat, *Journal of the American Chemical Society*, **2004**, 126, 4943-4950.
37. M. Thommes, *Chemie Ingenieur Technik*, **2010**, 82, 1059-1073.
38. Y.-C. Chiang, P.-C. Chiang and E.-E. Chang, *Chemosphere*, **1998**, 37, 237-247.
39. X. Wang, J. C. Yu, C. Ho, Y. Hou and X. Fu, *Langmuir*, **2005**, 21, 2552-2559.
40. N. Strataki, N. Boukos, F. Paloukis, S. G. Neophytides and P. Lianos, *Photochemical & Photobiological Sciences*, **2009**, 8, 639-643.
41. Y. Yang, C.-H. Chang and H. Idriss, *Applied Catalysis B: Environmental*, **2006**, 67, 217-222.
42. B. Zhou, M. Schulz, H. Lin, S. I. Shah, J. Qu and C. Huang, *Applied Catalysis B: Environmental*, **2009**, 92, 41-49.
43. D.-e. Gu, Y. Lu and B.-c. Yang, *Chemical Communications*, **2008**, 2453-2455.
44. A. Arvinte, M. Mahosenaho, M. Pinteala, A.-M. Sesay and V. Virtanen, *Microchimica Acta*, **2011**, 174, 337-343.
45. H.-F. Wang and Z.-P. Liu, *Journal of the American Chemical Society*, **2008**, 130, 10996-11004.

Table of contents entry

Soft-Template-Carbonization Route to Highly Textured Mesoporous Carbon-TiO_2 Inverse Opals for Efficient Photocatalytic and Photoelectrochemical Applications

Li Na Quan,[a] Yoon Hee Jang,[ab] Kelsey A. Stoerzinger,[c] Kevin J. May,[b] Yu Jin Jang,[a] Saji Thomas Kochuveedu,[a] Yang Shao-Horn[bc] and Dong Ha Kim*[ab]*

[a]Department of Chemistry and Nano Science, Global Top 5 Research Program, Division of Molecular and Life Sciences, College of Natural Sciences, Ewha Womans University, 52, Ewhayeodae-gil, Seodaemun-gu, Seoul 120-750, Korea

[b]Department of Mechanical Engineering, Massachusetts Institute of Technology, 77 Massachusetts Ave, Cambridge, Massachusetts 02139, United States

[c]Department of Materials Science and Engineering, Massachusetts Institute of Technology, 77 Massachusetts Ave, Cambridge, Massachusetts 02139, United States

*To whom correspondence should be addressed. E-mail: dhkim@ewha.ac.kr (D. H. Kim); shaohorn@mit.edu (Y. Shao-Horn)

Keywords: hybrid carbon-TiO_2, mesoporous inverse opal, photocatalyst, block copolymer, water splitting

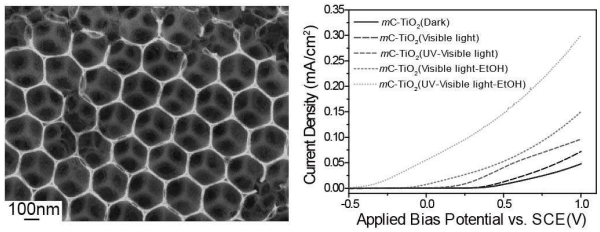

Highly ordered mesoporous carbon-TiO_2 inverse opal nanostructures provide maximized specific surface area and tunable electronic band gap energy, and they can optimize the transportation of matters and reduce transport limitations. A significantly enhanced visible light photocatalytic activity was demonstrated in terms of the degradation of *p*-nitrophenol (~79 %) and photoelectrochemical water splitting (~0.087 %).